PHOTONICS Research

Optimal illumination scheme for isotropic quantitative differential phase contrast microscopy

Yao Fan,[1,2,3,†] Jiasong Sun,[1,2,3,†] Qian Chen,[1,2,5] Xiangpeng Pan,[1,2,3] Lei Tian,[4] and Chao Zuo[1,2,3,*]

[1]School of Electronic and Optical Engineering, Nanjing University of Science and Technology, Nanjing 210094, China
[2]Jiangsu Key Laboratory of Spectral Imaging & Intelligent Sense, Nanjing University of Science and Technology, Nanjing 210094, China
[3]Smart Computational Imaging (SCI) Laboratory, Nanjing University of Science and Technology, Nanjing 210094, China
[4]Department of Electrical and Computer Engineering, Boston University, Boston, Massachusetts 02215, USA
[5]e-mail: chenqian@njust.edu.cn
*Corresponding author: zuochao@njust.edu.cn

Received 1 February 2019; revised 8 May 2019; accepted 9 June 2019; posted 10 June 2019 (Doc. ID 359414); published 26 July 2019

Differential phase contrast microscopy (DPC) provides high-resolution quantitative phase distribution of thin transparent samples under multi-axis asymmetric illuminations. Typically, illumination in DPC microscopic systems is designed with two-axis half-circle amplitude patterns, which, however, result in a non-isotropic phase contrast transfer function (PTF). Efforts have been made to achieve isotropic DPC by replacing the conventional half-circle illumination aperture with radially asymmetric patterns with three-axis illumination or gradient amplitude patterns with two-axis illumination. Nevertheless, the underlying theoretical mechanism of isotropic PTF has not been explored, and thus, the optimal illumination scheme cannot be determined. Furthermore, the frequency responses of the PTFs under these engineered illuminations have not been fully optimized, leading to suboptimal phase contrast and signal-to-noise ratio for phase reconstruction. In this paper, we provide a rigorous theoretical analysis about the necessary and sufficient conditions for DPC to achieve isotropic PTF. In addition, we derive the optimal illumination scheme to maximize the frequency response for both low and high frequencies (from 0 to $2NA_{obj}$) and meanwhile achieve perfectly isotropic PTF with only two-axis intensity measurements. We present the derivation, implementation, simulation, and experimental results demonstrating the superiority of our method over existing illumination schemes in both the phase reconstruction accuracy and noise-robustness.

https://doi.org/10.1364/PRJ.7.000890

1. INTRODUCTION

Quantitative phase imaging (QPI), which provides phase information about the refractive index distribution of transparent specimens, has drawn much attention in both optical and biomedical research [1–3]. The major advantage of QPI over conventional intensity imaging or fluorescence microscopy is that it requires no exogenous contrast agents (e.g., dyes or fluorescent protein) to enhance the contrast of the microscopic image, which enables label-free and stain-free optical imaging of live biological specimens *in vitro* [4,5]. The most common QPI methods are based on interferometry and holography with coherent illumination and a reference beam, making them expensive and sensitive to misalignment, vibrations, and speckle noise [6–8]. To overcome these limitations, non-interferometric QPI approaches using partially coherent illumination have been developed, such as transport-of-intensity equation (TIE) [2,9–14], differential phase contrast microscopy (DPC) [15–20], and Fourier ptychographic microscopy (FPM) [21–25]. TIE is a well-established non-interferometric phase retrieval approach, which enables the QPI of a transparent sample simply by measuring the intensities at multiple axially displaced planes [2,9,11–14]. The advantages of the TIE approach are that it is fully compatible with widely available bright-field microscopy hardware and able to offer an imaging resolution up to the incoherent resolution limit (two times better than the coherent diffraction limit) under matched annular illumination [26,27]. Without moving the position of a sample, DPC and FPM approaches retrieve the complex field of the sample by using asymmetric illuminations. In FPM, a set of low-resolution (LR) intensity images corresponding to different illumination angles, with the resolution determined by the numerical aperture (NA) of the objective lens, are acquired [21,22,24,25]. These LR intensity images are iteratively combined together in the Fourier

domain, resulting in a wide-field, high-resolution complex image with the synthesized resolution determined by the sum of the objective lens and illumination NAs [21–25,28,29]. DPC, however, achieves phase recovery by using only four images with asymmetric illuminations in opposite directions [18,19]. It converts invisible sample phases into measurable intensity by shifting the sample's spectrum in Fourier space to theoretically achieve a resolution of twice the coherent diffraction limit [18,19]. Assuming a linearized model for a weakly scattering sample, the DPC phase retrieval problem becomes a single-step deconvolution process using the phase contrast transfer function (PTF). By implementing DPC with a programable LED array [19,20,30] or a programable LCD panel [31], we are able to realize dynamic QPI along arbitrary axes of asymmetry, without any mechanical moving parts.

To recover the quantitative phase information of a weakly scattering sample, at least two complementary source patterns are required in DPC. However, the resultant PTF is antisymmetric and zero at all spatial frequencies along the axis of asymmetry, which may lead to significant phase reconstruction artifacts if not properly handled. So in general, the illumination of DPC is designed with two-axis half-circle amplitude patterns, that is, four patterns (top, bottom, left, right half-circles) are used to avoid missing frequencies. However, artifacts of phase reconstruction still cannot be completely avoided, since DPC's PTF is not circularly symmetric with only two-axis measurements. Recently, efforts have been made toward developing high-speed, or even single-shot QPI mechanisms, such as motion compensation and color-coded DPC based on wavelength multiplexing [30,32–34]. Other efforts have been made to improve the phase reconstruction quality of DPC by optimizing the illumination scheme, phase reconstruction algorithm, and compensating for aberrations, and so on [35–39]. Among these methods, optimizing illumination becomes the most direct and effective approach to improve the image quality of DPC since the PTF of DPC is directly determined by illumination. By using three-axis radially asymmetric patterns [35] or two-axis gradient amplitude patterns [36] instead of more time-consuming intensity measurements along different illumination angles (12-axis) [20], the isotropic DPC is achieved with higher imaging efficiency. The machine learning is also introduced to the DPC illumination design, which improves the phase recovery accuracy, while reducing the raw intensity measurements at the same time [38]. Although the transfer response and isotropy of the PTF improved, the underlying theoretical mechanism of isotropic PTF has not been explored, so the optimal illumination scheme cannot be determined. Furthermore, the frequency responses of the PTFs under these engineered illuminations have not been fully optimized, leading to suboptimal phase contrast and signal-to-noise ratio (SNR) for phase reconstruction.

In this paper, we improve on these works by providing a rigorous theory for achieving isotropic DPC, where a new optimal illumination scheme is derived. The major advantages of the new illumination scheme are twofold. First, it is able to produce a circularly symmetrical PTF with only two-axis intensity measurements under partially coherent condition. Thus, it is expected to achieve high-quality phase reconstruction with isotropic transverse resolution and SNR by using only four intensity measurements. Second, the resulting PTF achieves a broadband frequency coverage for partially coherent imaging (from 0 to $2\mathrm{NA}_{\mathrm{obj}}$) with a smooth and significantly enhanced response for both low and high frequencies, which alleviates the ill-posedness of the PTF inversion.

2. OPTIMAL ILLUMINATION SCHEME DESIGN

A. Derivation of Generalized Illumination Function for Isotropic Differential Phase Contrast

Consider a weak-scattering object with complex transmission function $t(\mathbf{r}) = e^{-a(\mathbf{r})+i\phi(\mathbf{r})}$, illuminated by an oblique plane wave with a uniform intensity distribution $S(\mathbf{u_j})$ ($\mathbf{u_j}$ denotes the spatial frequency of the tilted illumination). Invoking the weak object approximation $t(\mathbf{r}) \approx 1 - a(\mathbf{r}) + i\phi(\mathbf{r})$ [40,41], the intensity spectrum of the bright-field image under oblique illumination can be separated into three terms [42], including the background, absorption contrast, and phase contrast terms (ignore systematic aberrations):

$$\begin{aligned} I_j(\mathbf{u}) = {} & S(\mathbf{u_j})\delta(\mathbf{u})|P(\mathbf{u_j})|^2 \\ & - S(\mathbf{u_j})A(\mathbf{u})[P^*(\mathbf{u_j})P(\mathbf{u}+\mathbf{u_j}) + P(\mathbf{u_j})P^*(\mathbf{u}-\mathbf{u_j})] \\ & + iS(\mathbf{u_j})\Phi(\mathbf{u})[P^*(\mathbf{u_j})P(\mathbf{u}+\mathbf{u_j}) - P(\mathbf{u_j})P^*(\mathbf{u}-\mathbf{u_j})], \end{aligned} \tag{1}$$

where $P(\mathbf{u})$ denotes the pupil function of the objective lens (assuming it is an ideal low-pass filter with a cutoff frequency of $\frac{\mathrm{NA}_{\mathrm{obj}}}{\lambda}$), and $A(\mathbf{u})$ and $\Phi(\mathbf{u})$ are the Fourier transform of the sample's absorption and phase function, respectively. To generate the phase contrast image I_{lr}^{DPC} (e.g., the left–right DPC) along a specific direction of the phase gradient, a pair of images where each $S(\mathbf{u})$ has complementary gradient vector are used to calculate $I_{lr}^{\mathrm{DPC}} = \frac{I_r - I_l}{I_r + I_l}$ [18,41]. Since two illumination patterns are symmetrical along the same axial direction (e.g., x-axis in left–right DPC), the background term and absorption contrast term are cancelled, leaving only the phase contrast term. So, the corresponding PTF of the left–right DPC can be expressed as

$$\mathrm{PTF}_{lr}(\mathbf{u}) = \frac{\iint S_{lr}(\mathbf{u_j})[P^*(\mathbf{u_j})P(\mathbf{u}+\mathbf{u_j}) - P(\mathbf{u_j})P^*(\mathbf{u}-\mathbf{u_j})]\mathrm{d}^2\mathbf{u_j}}{\iint |S_{lr}(\mathbf{u_j})||P(\mathbf{u_j})|^2\mathrm{d}^2\mathbf{u_j}}. \tag{2}$$

It can be found from Eq. (2) that once the optical configuration of the microscope is fixed (the pupil function of the objective lens is predefined), the PTF is fully determined by the illumination function [43].

To reconstruct the sample's quantitative phase information from Eq. (2), we can solve the inverse problem with a single-step deconvolution [20]. Tikhonov regularization parameter β is often introduced in the denominator to avoid singularity in the PTF inversion [44]:

$$\phi(\mathbf{r}) = \mathcal{F}^{-1}\left\{\frac{\sum_i [\mathrm{PTF}_i^*(\mathbf{u}) \cdot I_i^{\mathrm{DPC}}(\mathbf{u})]}{\sum_i |\mathrm{PTF}_i^*(\mathbf{u})|^2 + \beta}\right\}, \tag{3}$$

where $\mathrm{PTF}_i^*(\mathbf{u})$ denotes complex conjugation of PTF along different axial directions. The denominator term $\sum_i |\mathrm{PTF}_i^*(\mathbf{u})|^2$ represents the synthetic square of amplitude of the multi-axial PTFs, which can be used to indicate the degree of isotropy for

DPC imaging. For simplicity, we use a shorthand notation $C(\mathbf{u})$ for this term in the following analysis.

The following derivation about isotropic DPC is performed in the polar coordinate instead of the Cartesian coordinate; that is, we use (ρ,θ) instead of (x,y), where ρ and θ respectively represent the radius and the polar angle. This is because the optical systems have circular symmetry, and most circularly symmetric functions are separable in their polar coordinates, i.e., we can write $S_{lr}(\rho,\theta)$ and $S_{ud}(\rho,\theta)$ as a product of two one-dimensional functions about ρ and θ, respectively:

$$\begin{aligned} S_{lr}(\rho,\theta) &= L(\rho)M(\theta), \\ S_{ud}(\rho,\theta) &= L(\rho)N(\theta). \end{aligned} \tag{4}$$

Since the phase contrast image is generated by complementary illumination in each axis measurement $S_{lr} = S_r - S_l$, the illumination function $S_{lr}(\rho,\theta)$ is an even function about θ. Similarly, the illumination function $S_{ud}(\rho,\theta)$ for the up–down axis is an odd function about θ. Thus, $M(\theta)$ and $N(\theta)$ can be further expanded in the Fourier series defined on $(-\pi, \pi]$:

$$\begin{aligned} M(\theta) &= \sum_{n=1}^{\infty} a_n \cos(n\theta), \\ N(\theta) &= \sum_{n=1}^{\infty} b_n \sin(n\theta). \end{aligned} \tag{5}$$

For general illumination and aperture function, the PTF can be calculated by integrating the overlapping areas between the objective pupil function (with its center at the origin O) and its off-axis version (with its center at the point Q), as illustrated by the red and blue regions in Fig. 1. This is because the illumination falling in the red regions can ensure the point Q is within $P(\mathbf{u}+\mathbf{u_j}) = 1$, and the illumination falling in the blue regions can ensure the point $Q(\mathbf{u})$ is within $P(\mathbf{u}-\mathbf{u_j}) = 1$. However, it should be noted that when the illumination angle is close to the central axis of the objective lens, the two red and blue regions corresponding to $P(\mathbf{u}+\mathbf{u_j})$ and $P(\mathbf{u}-\mathbf{u_j})$ will be partially cancelled out by each other. So the integral interval should be partitioned according to the location of point Q [see Figs. 1(a) and 1(b)], which can be represented as (taking left–right axis illumination for example)

$$\mathrm{PTF}_{lr}(\rho,\theta) = \begin{cases} \dfrac{2\int_{\rho-\mathrm{NA_{obj}}}^{\mathrm{NA_{obj}}}\int_{\theta-\alpha}^{\theta+\alpha} S_{lr}(\xi,\varepsilon)\mathrm{d}\varepsilon\mathrm{d}\xi}{\int_0^{\mathrm{NA_{obj}}}\int_0^{2\pi}|S_{lr}(\xi,\varepsilon)|\mathrm{d}\varepsilon\mathrm{d}\xi} & \mathrm{NA_{obj}} \le \rho \le 2\mathrm{NA_{obj}} \\ \dfrac{2\int_{\mathrm{NA_{obj}}-\rho}^{\mathrm{NA_{obj}}}\int_{\theta-\alpha}^{\theta+\alpha} S_{lr}(\xi,\varepsilon)\mathrm{d}\varepsilon\mathrm{d}\xi}{\int_0^{\mathrm{NA_{obj}}}\int_0^{2\pi}|S_{lr}(\xi,\varepsilon)|\mathrm{d}\varepsilon\mathrm{d}\xi} & 0 \le \rho < \mathrm{NA_{obj}} \end{cases}. \tag{6}$$

Substituting Eqs. (4) and (5) into Eq. (6) gives the PTF along the left–right axis direction. Although the mathematical formulas appear complicated, we should keep in mind that to achieve isotropic DPC, it is only required that the synthetic square of amplitude of the multi-axial PTFs $C(\rho,\theta)$ $[C(\rho,\theta) = |\mathrm{PTF}_{lr}(\rho,\theta)|^2 + |\mathrm{PTF}_{ud}(\rho,\theta)|^2]$ is only a function of ρ. Close inspection of Eq. (6) reveals that the isotropy cannot be achieved if there are cross-trigonometric terms in $C(\rho,\theta)$, suggesting there should be only one single-harmonic component in the Fourier series expansion of Eq. (5), that is (see Appendix A for detailed derivation):

$$\begin{aligned} S_{lr}(\rho,\theta) &= L(\rho)\cos(n\theta) \\ S_{ud}(\rho,\theta) &= L(\rho)\sin(n\theta) \end{aligned} \quad (n = 1,3,5,\ldots). \tag{7}$$

Note that in Eq. (7), we neglect the unimportant constant factors. It should be further noted that when n is even, the illumination pattern is centrosymmetric so that the resulting PTF will be completely canceled out. Therefore, n should be an odd number $(n = 1,3,5,\ldots)$ to guarantee a valid non-zero PTF. Equation (7) is the main result of our work, which provides the necessary and sufficient conditions for DPC to achieve isotropic PTF.

B. Optimal Illumination Scheme

Since no restrictions were imposed on the form of the function $L(\rho)$, $L(\rho)$ can be any function of ρ without affecting the isotropy of the DPC's PTF. Thus, we can optimize the function $L(\rho)$ to improve the frequency coverage and response of the corresponding PTF. In our recent studies, an annular source has been demonstrated that optimizes the PTF of DPC [45],

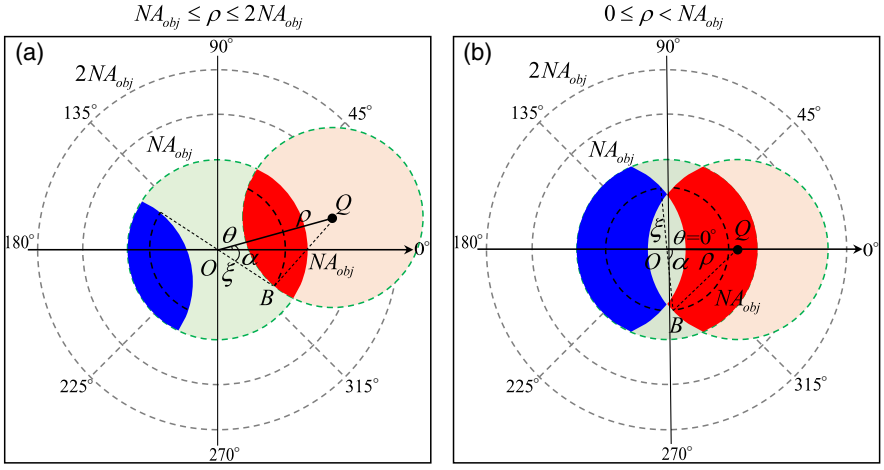

Fig. 1. Schematic diagram of the integral for PTF along the left–right axis in the polar coordinate system. (a) The radius ρ of the point Q is in the range of $\mathrm{NA_{obj}} \le \rho \le 2\mathrm{NA_{obj}}$. (b) The radius ρ of the point Q is in the range of $0 \le \rho < \mathrm{NA_{obj}}$.

TIE [26,27], and FPM [28,42]. In this paper, the annular source is also used in the generalized illumination function of isotropic DPC to optimize the transfer response of PTF. In Appendix B, we compare the resultant PTFs of three different functions $L(\rho)$: constant weight, linear weight, and Kronecker delta weight functions with a fixed $n = 1$ by simulation. The results suggest that the delta weight function (a thin annulus) produces the PTF with the highest response at almost all frequencies from 0 to $2\mathrm{NA}_{\mathrm{obj}}$.

To further analyze the influence of the thickness of the annulus on the PTF, we illustrate the corresponding PTFs of different annular thickness by fixing the NA of the outer circles to be $\mathrm{NA}_{\mathrm{obj}}$ and by only changing the thickness of the annulus. As might be expected, the phase contrast is gradually reduced as the annulus width increases, especially at low and high frequencies. This is because the paraxial illumination does not produce low-frequency phase contrast, and only illumination matching the objective $\mathrm{NA}_{\mathrm{obj}}$ can produce the strong response at all frequencies. Specific simulations and comparisons can be found in Appendix C. When the thickness of the annulus is extremely small ($\sigma = \frac{\mathrm{NA}_{\mathrm{ill}}}{\mathrm{NA}_{\mathrm{obj}}} \to 0$), the phase response finally approaches that of the constant weight function $L(\rho) = 1$. From the results in Appendix C, it can be deduced that we should choose the diameter of the annulus to be equal to that of the objective pupil and make its thickness as small as possible [$\delta(\rho - \mathrm{NA}_{\mathrm{obj}})$, where $\delta(\rho)$ is the delta function] to optimize the response of PTF.

Finally, we study the effect of the number n in Eq. (7) on the PTF. Three odd n numbers are selected to generate three illumination patterns and corresponding PTFs (see Appendix D). It is shown that when n increases ($n = 3, 5$), not only the PTF response is significantly attenuated, but also the number of zero crossings in $C(\rho, \theta)$ increases. In such cases, the reconstruction phase can be severely distorted due to the ill-posedness of the PTF inversion. Thus, $n = 1$ provides the optimal PTF for DPC with the strongest response and no zero crossings from 0 to $2\mathrm{NA}_{\mathrm{obj}}$. Based on the above analysis, the optimal illumination scheme for isotropic DPC can be represented as

$$\begin{aligned} S_{lr}(\rho, \theta) &= \delta(\rho - \mathrm{NA}_{\mathrm{obj}}) \cos\theta, \\ S_{ud}(\rho, \theta) &= \delta(\rho - \mathrm{NA}_{\mathrm{obj}}) \sin\theta. \end{aligned} \tag{8}$$

Meanwhile, we can also give the analytical expressions of PTF under the optimal illumination scheme:

$$\begin{aligned} \mathrm{PTF}_{lr}(\rho, \theta) &= \sin\alpha \cos\theta, \\ \mathrm{PTF}_{ud}(\rho, \theta) &= \sin\alpha \sin\theta. \end{aligned} \tag{9}$$

Based on the geometric relationship of the isosceles triangle BOQ in Fig. 1, α is determined by $\cos\alpha = \frac{\rho}{2\mathrm{NA}_{\mathrm{obj}}}$. In this case, $C(\rho, \theta)$ can be calculated as

$$C(\rho, \theta) = 1 - \frac{\rho^2}{4\mathrm{NA}_{\mathrm{obj}}^2}. \tag{10}$$

Equation (10) indicates that $C(\rho, \theta)$ is only related to ρ, which means that the corresponding PTF of DPC is isotropic.

3. IMAGING PERFORMANCE OF OPTIMAL ILLUMINATION SCHEME

To verify the isotropy of the optimal illumination scheme, we numerically simulated PTFs and $C(\rho, \theta)$ for four DPC illumination patterns under two-axis illumination, including three states of the arts, namely uniform illumination [20], (two-axis) radial illumination [35], gradient amplitude illumination [36], and the optimal illumination proposed in this work, as shown in Fig. 2. In Figs. 2(b1)–2(b4), we show PTFs along the left–right axis under these different illumination patterns. It can be observed that the PTF under optimal illumination scheme has a smooth and significantly enhanced response at almost all frequencies of the theoretical bandwidth of the entire partially coherent imaging (from 0 to $2\mathrm{NA}_{\mathrm{obj}}$). These can be seen more clearly from the amplitude of $C(\rho, \theta)$ in Figs. 2(c1)–2(c4), where the $C(\rho, \theta)$ under the optimal illumination scheme has obviously enhanced values at the low-frequency components near the zero frequency and the high-frequency components approaching $2\mathrm{NA}_{\mathrm{obj}}$.

To quantitatively compare these four PTFs, the black cross-section in Fig. 2(c1) is used to characterize the amplitude of $C(\rho, \theta)$. As shown in Fig. 2(d), the optimal illumination scheme has the maximum phase contrast at almost all frequencies from 0 to $2\mathrm{NA}_{\mathrm{obj}}$. Moreover, the peak values of $C(\rho, \theta)$ for the other three illumination patterns are below 0.9, while they can reach 1 under the optimal illumination scheme. The strong phase contrast under the optimal illumination can be finally converted to the quantitative phase images by the PTF inversion, resulting in high-quality reconstructions with a uniform background and an improved resolution. To compare the degree of isotropy, we further plotted the values along three different concentric circles within $C(\rho, \theta)$ in Figs. 2(e1)–2(e3). A constant frequency response can be obtained along the circle under the gradient amplitude illumination and the optimal illumination scheme, suggesting that $C(\rho, \theta)$ obtained under these two illumination patterns are isotropic, while the uniform illumination [20] and the radial illumination [35] cannot generate isotropic PTFs under two-axis illumination due to their fluctuant frequency responses along the concentric circles.

The proposed optimal illumination scheme is then compared with different illumination patterns based on simulations. The Siemens star image [shown in Fig. 3(a)] [46] is used as an example phase object that is defined on a grid with 244 × 244 pixels with a pixel size of 0.2 μm × 0.2 μm. The wavelength of the illumination is 525 nm, and the $\mathrm{NA}_{\mathrm{obj}}$ is 0.40. For such an imaging configuration, the ideal phase imaging resolution that can be achieved is 656 nm ($\lambda/2\mathrm{NA}_{\mathrm{obj}}$), which is also shown in Fig. 3(b). For partially coherent image calculation, we use the Abbe's method, in which each sub-image corresponding to point source in the aperture plane is superimposed at the image plane to generate captured images of DPC. To simulate the noise effect, each DPC image is corrupted by Gaussian noise with a standard deviation of 0.0003. In Fig. 3, we compare the phase retrieval results of different illumination patterns for different regularization conditions. For the case without regularization (β is an infinitesimal), the noise corresponding to the frequency components with extremely weak PTF responses was amplified,

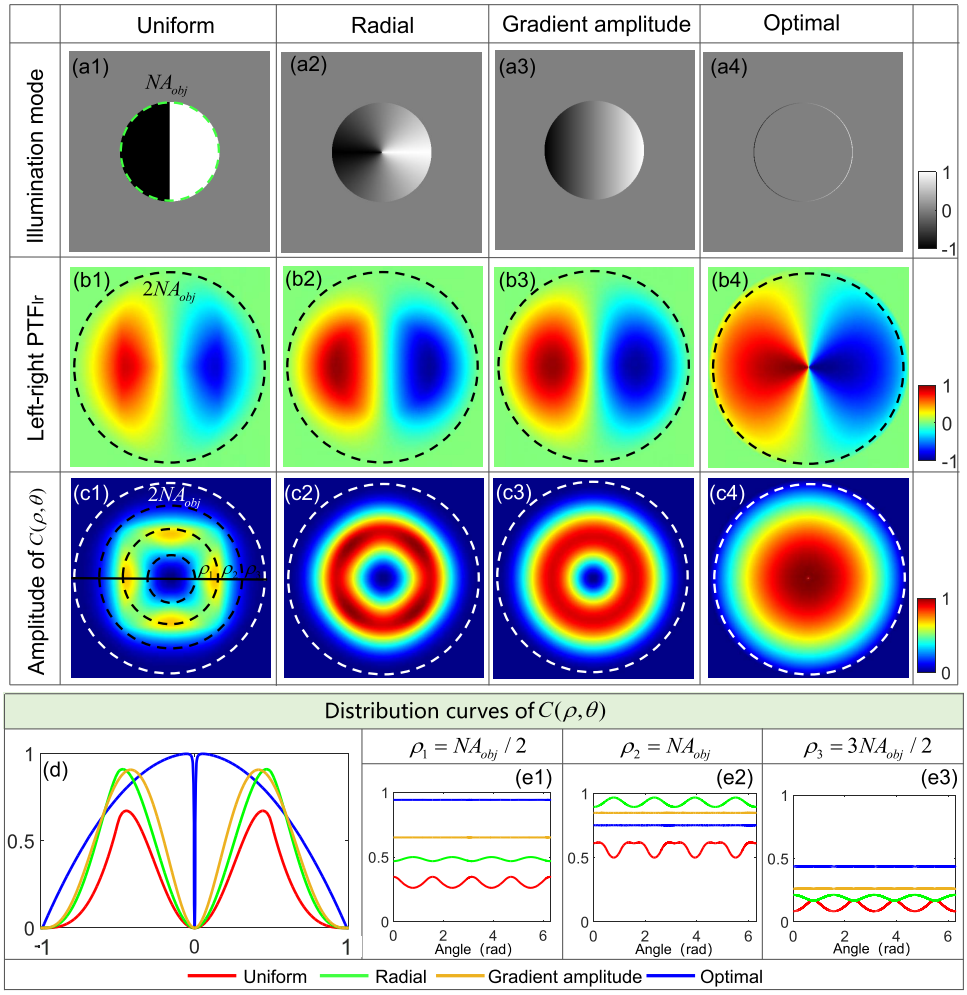

Fig. 2. PTF and $C(\rho,\theta)$ with four illumination patterns. (a1)–(a4) Four illumination patterns. (b1)–(b4) PTFs along the left–right axis. (c1)–(c4) $C(\rho,\theta)$ with two-axis illumination. (d) Quantitative curves of $C(\rho,\theta)$ along the black straight line under the four illumination patterns. (e1)–(e3) Quantitative curves of $C(\rho,\theta)$ under the four illumination patterns on three radii.

resulting in grainy artifacts superimposed on the reconstructed phases by using uniform illumination [20], (two-axis) radial illumination [35], and gradient amplitude illumination [36] [Figs. 3(c1)–3(c3)]. To stabilize the deconvolution process, a regularization parameter β is generally introduced to the denominator of Eq. (3) to suppress the noise effect. As shown in Figs. 3(d1)–3(d3), when $\beta = 0.2$, the grainy artifacts are significantly reduced under these three illumination patterns, but meanwhile, the low-frequency phase values are underestimated, and high-frequency features are significantly attenuated. Thus, a more properly chosen regularization parameter is required for these illumination patterns to achieve reliable phase reconstructions under noisy conditions. In contrast, the proposed optimal illumination scheme can always obtain accurate and high-quality reconstructed phases with any regularization parameters attributed to its significantly enhanced PTF response from the 0 to $2NA_{obj}$ range [Fig. 2(b4)], as shown in Figs. 3(c4) and 3(d4). The root-mean-square error (RMSE) values for the optimal illumination DPC are compared with the other illumination patterns to quantitatively measure the SNR of these reconstructed phases. It can be found that the reconstructed phase under the optimal illumination always achieves the lowest RMSE values.

To verify the isotropy of the DPC phase reconstruction under the optimal illumination scheme, phase values along three small circles corresponding to different spatial frequencies evenly distributed from 0 to $2NA_{obj}$ are extracted and plotted in Fig. 3(e) (the black curve denotes the ground truth, and the red, green, and blue curves represent the low frequency, middle frequency, and high frequency, respectively). From these curves, the line widths corresponding to different frequency components can be clearly distinguished at all angles, which indicates that optimal illumination achieves an isotropic resolution at all spatial frequencies. In addition, it can be observed that the reconstructed phase contrast under optimal illumination is close to the ground truth phase. Furthermore, to quantitatively compare the resolution of DPC reconstruction results of these four illumination patterns, we then extracted and plotted the phase values along a small circle of the same radius in

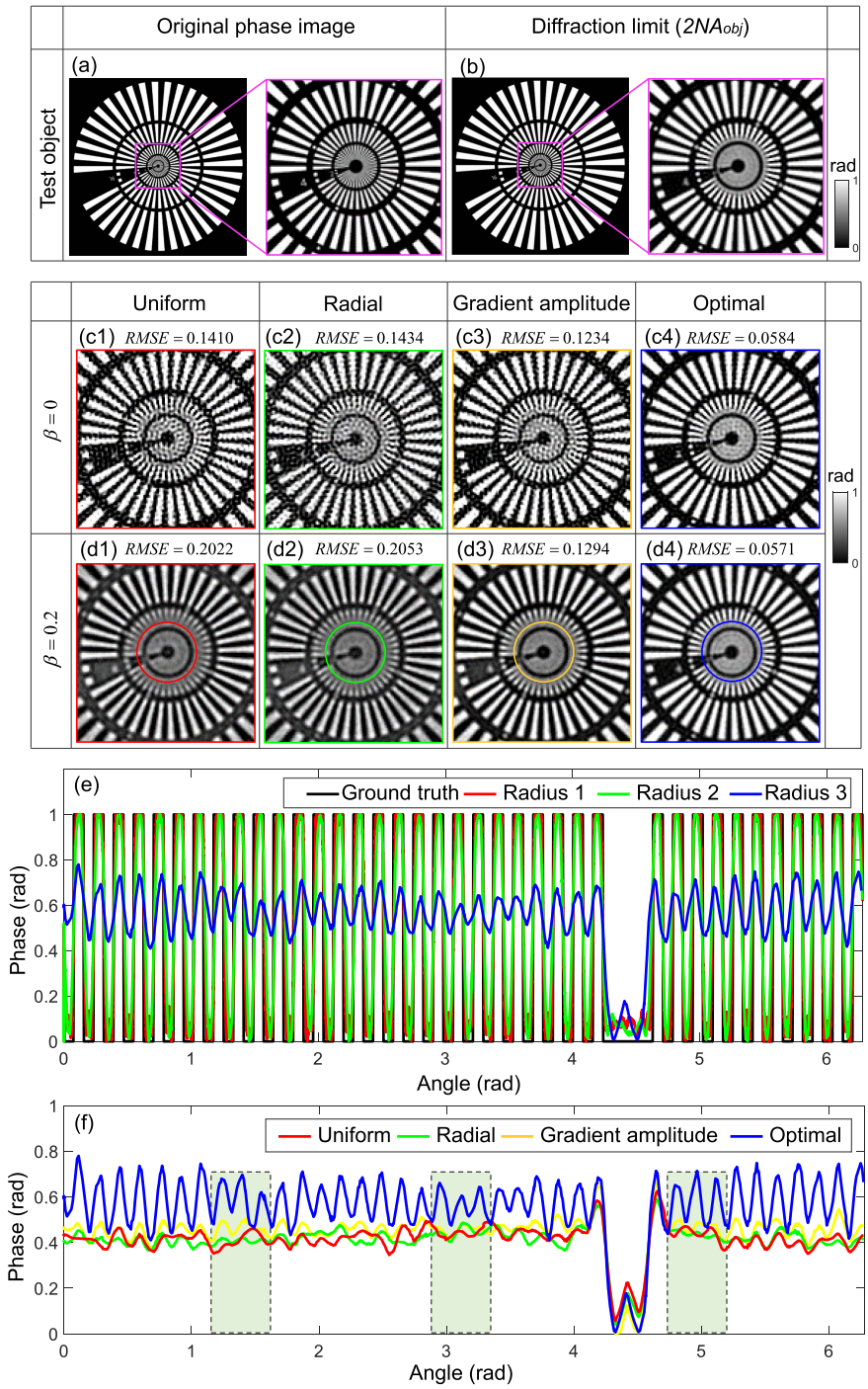

Fig. 3. Simulation results with different regularization parameters under four illumination patterns. (a) Original phase image. (b) Diffraction limit phase image of DPC ($2NA_{obj}$). (c1)–(c4), (d1)–(d4) Phase results with regularization parameters of 0 and 0.2. (e) Phase values along three small circles corresponding to different spatial frequencies evenly distributed from 0 to $2NA_{obj}$. (f) Phase values along a small circle of the same radius in (d1)–(d4) under four illumination patterns.

Figs. 3(d1)–3(d4). As shown in Fig. 3(f), the uniform, radial, and gradient amplitude illuminations all produce results with underestimated phase contrast (phase amplitude 0.1). In contrast, the phase amplitude is stabilized around 0.4 under our optimal illumination, which is closer to the ground truth. Moreover, it can be seen that the phase detail in the green marked regions, which corresponds to the weak PTF frequency responses under the uniform and radial illumination patterns, cannot be recovered correctly. However, the optimal illumination scheme achieves an isotropic resolution, as well as much more accurate phase values, due to its isotropic PTF with much stronger responses.

4. EXPERIMENTAL RESULTS

A. Phase Resolution Target

To verify the effectiveness of the optimal illumination scheme experimentally, we first measured a pure phase resolution target [Quantitative Phase Microscopy Target (QPT^{TM}), Benchmark Technologies Corporation, USA]. Our setup was based on a commercial inverted microscope (IX83, Olympus), in which the original condenser diaphragm is replaced by a high-contrast an amorphous silicon (a-Si) thin-film transistor LCD screen [4.3 inch (1 inch = 2.54 cm), pixel resolution 480 × 272] [47]. In our experiments, the built-in halogen white light source with a green interference filter (central wavelength $\lambda = 550$ nm, 45 nm bandwidth) was used for illumination, and the LCD screen was used to modulate the illumination in asymmetrical manners. The images were captured by an objective lens with a magnification of 10× and an NA of 0.25 (Olympus PLAN 10X/0.25), and finally digitalized by a charge coupled device (CCD) camera with the pixel size of 3.75 μm (the imaging source DMK 23U445). Figure 4(a) shows a bright-field image captured when the LCD screen is transparent, which has very little intensity contrast. To illustrate the imaging resolution more clearly, the small regions near the center of the image (green-boxed areas) of the reconstructed phases under the half-circular uniform illumination and optimal illumination schemes are shown in Figs. 4(c) and 4(d). In the reconstruction phase of Fig. 4(c), two more suitable regularization parameters are used to suppress low-frequency and high-frequency errors, respectively. To demonstrate the isotropy of the optimal illumination scheme, the phase values at three uniformly distributed frequencies of Fig. 4(d) are extracted to plot the quantitative curves. As shown in Fig. 4(e), the optimal illumination achieves isotropic resolution at different frequencies. Furthermore, line profiles along a small circle of the same radius (blue and red circles) are extracted and

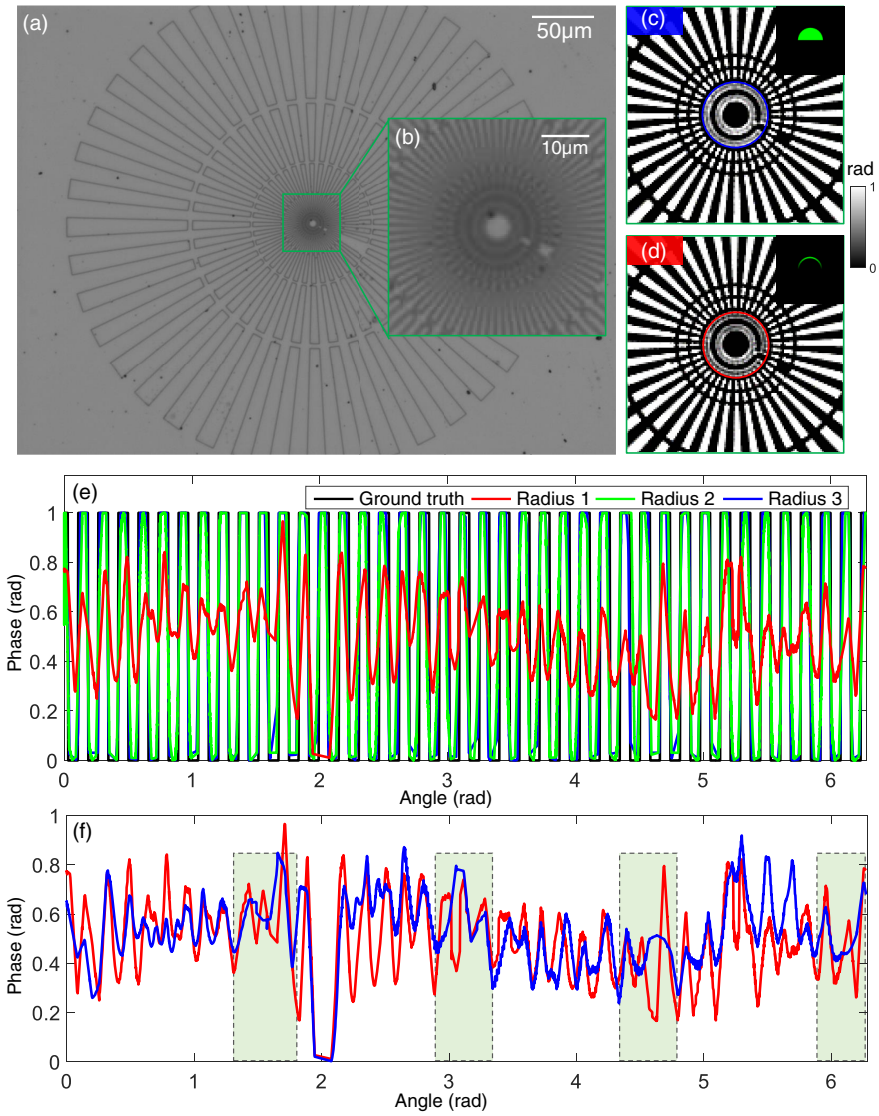

Fig. 4. Phase reconstruction results of a phase resolution target QPT^{TM}. (a) A bright-field image. (b) A zoom-in of the interest region of the bright-field image. (c) Phase reconstruction result under the half-circular uniform illumination pattern. (d) Phase reconstruction result under the optimal illumination scheme. (d) Phase values along three small circles evenly distributed from 0 to $2NA_{obj}$ under the optimal illumination pattern. (e) Phase values along a small circle of the same radius in (c), (d) under the half-circular uniform illumination pattern and optimal illumination pattern.

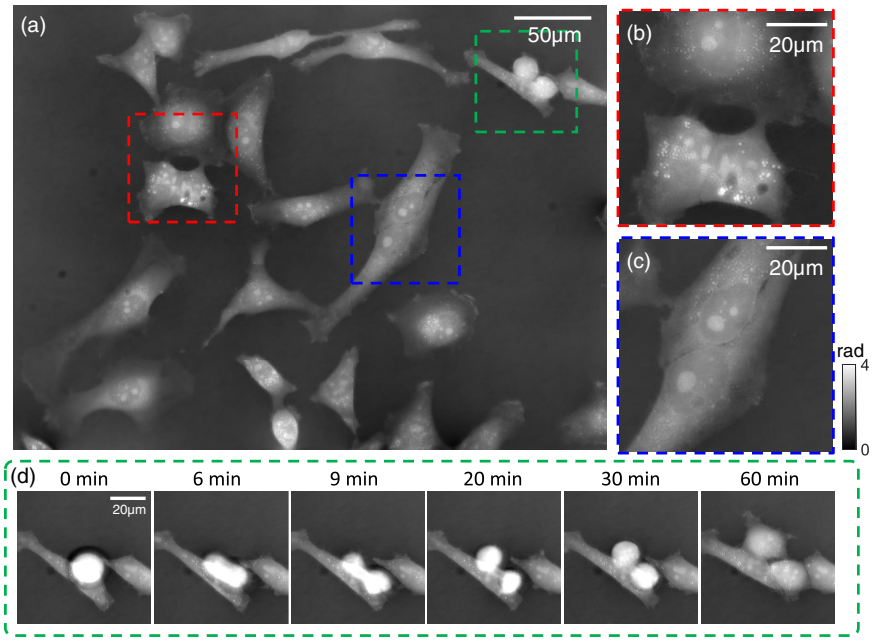

Fig. 5. Phase reconstruction results of HeLa cells under the optimal illumination scheme. (a) Full-field-of-view phase distribution. (b), (c) Phase maps of two selected zooms. (d) Phase results at different time points.

illustrated in Fig. 4(f) to quantitatively compare the highest achievable resolution. These results are generally consistent with the theoretical prediction, as well as our simulation results. It can be seen that the phase details in the green areas, which correspond to the frequency components with weak responses in the non-isotropic PTF of the uniform illumination pattern, cannot be recovered correctly, indicating that half-circular uniform illumination cannot provide phase reconstruction with isotropic transverse resolution and SNR. Once again, the phase reconstruction result obtained by using the optimal illumination scheme demonstrates much better isotropy.

B. Unstained HeLa Cells

The high-resolution QPI capability of the proposed optimal illumination scheme provides unique possibilities for the label-free imaging of cell growth in culture, using repeated imaging of cultures to assess the progression toward confluence over designated periods of time. In Fig. 5, we show the quantitative phase images of the human cervical adenocarcinoma epithelial (HeLa) cell division process over the course of 5 h. The experimental setup generally followed the parameters of the previous experiment, except that an objective lens with 10×, 0.4 NA (Olympus UPlanSApo 10X/0.4) and an additional 1.25× camera adapter were used (effective magnification 12.5×). A time-lapse movie created with one-phase reconstruction per 22 s is provided in Visualization 1. We show the full-field-of-view phase reconstruction result in this video [one frame from the video is shown in Fig. 5(a)]. From two selected zoom-in regions (red-boxed and blue-boxed areas) in Figs. 5(b) and 5(c), subcellular features, such as cytoplasmic vesicles and pseudopodium, can be clearly observed. In Fig. 5(d), we further selected one cell [corresponding to the green-boxed region shown in Fig. 5(a)] to study its morphology during division, which spanned over about 1 h. These high-resolution phase images clearly reveal the cell morphological changes during different mitosis phases. In addition, since the optimal illumination scheme requires only two-axis illuminations, all these retracting, extending, reorganizing, migrating, and maturing processes of the cell(s) were recovered accurately without any motion blur. These results demonstrate that the optimal illumination scheme is capable of imaging unlabeled cells in a non-invasive manner, allowing for a high-resolution QPI over an extended period of time.

5. DISCUSSION AND CONCLUSIONS

In this work, a rigorous theoretical analysis about the necessary and sufficient conditions for DPC to achieve an isotropic PTF has been explored. We have derived an optimal illumination scheme to maximize the frequency response and meanwhile achieve isotropic DPC. Compared with a traditional DPC method that uses half-circle illumination, our optimal illumination scheme produces a perfectly circularly symmetrical PTF with only two-axis intensity measurements, avoids missing frequencies, and enhances the phase response, providing high-quality phase reconstruction with isotropic transverse resolution and SNR. The resultant PTF removes the ill-posedness of the PTF inversion so that artifacts in phase reconstruction results can be significantly reduced. A theoretical analysis, simulations, and experimental results have verified the superiority of our method over existing illuminations in both the phase reconstruction accuracy and noise-robustness. The investigation of live HeLa cell mitosis *in vitro* has demonstrated that our optimal DPC scheme is a simple, efficient, and stable approach for label-free quantitative cell imaging with subcellular resolution. Furthermore, the intrinsic advantages, such as being

non-interferometric, having the compatibility with bright-field microscopic hardware, and incoherent diffraction-limited resolution up to $2NA_{obj}$, make it a competitive and promising technique for various microscopy applications in life sciences and biophotonics.

In this work, we derived the optimal illumination scheme in an ideal imaging system. It should be noted that the actual imaging system is often more complicated due to the aberrations and noise. Several studies have improved the imaging performance of DPC from other aspects, such as the optimized reconstruction algorithm, regularization algorithm, and aberration compensation [38,39]. In this paper, to make a fair comparison, we adopted the most common and the simplest algorithm to ensure that the improvement of the phase quality can only result from the illumination optimization. In Appendix E, it is demonstrated that the optimal illumination can still achieve stable high-quality imaging results in an imaging system with a small aberration. In essence, the optimal illumination scheme can be combined with other optimized compensation approaches to further improve the phase reconstruction quality of DPC. On the other hand, compared with the existing 12-axis and three-axis method, the optimal scheme improves the imaging speed while ensuring the isotropic, but does not exceed the imaging speed of the traditional two-axis DPC. When imaging rapidly varying samples, the optimal illumination cannot completely avoid motion artifacts. Combining our approach with color-multiplexing techniques to achieve single-shot isotropic DPC imaging can potentially solve this problem, which is an interesting direction for future work.

APPENDIX A: DERIVATION OF ISOTROPIC DPC UNDER GENERALIZED ILLUMINATION CONDITIONS

In this section, we present the rigorous theoretical analysis about the necessary and sufficient conditions for DPC to achieve a perfectly isotropic PTF under generalized illumination conditions. As presented in Fig. 6, we show the schematic diagram of the integral for PTF along the left–right axis illumination in the polar coordinate system. Since the phase contrast image is generated by complementary illumination in each axis measurement $S_{lr} = S_r - S_l$, the illumination function $S_{lr}(\rho,\theta)$ can be expressed as a periodic even function about θ. Similarly, we can get the illumination function $S_{ud}(\rho,\theta)$ in the up–down axis direction as a periodic odd function about θ. Thus, $S_{lr}(\rho,\theta)$ and $S_{ud}(\rho,\theta)$ can be expanded in the Fourier series defined on $(-\pi,\pi)$:

$$S_{lr}(\rho,\theta) = L(\rho)\sum_{n=1}^{\infty} a_n \cos(n\theta),$$
$$S_{ud}(\rho,\theta) = L(\rho)\sum_{n=1}^{\infty} b_n \sin(n\theta), \tag{A1}$$

where a_n and b_n are a series of constants, and $L(\rho)$ is a function about radius ρ.

For the general illumination and aperture function, the PTF can be calculated by integrating the overlapping areas between the objective pupil function (with its center at the origin O) and its off-axis version (with its center at the point Q), as illustrated by the red and blue regions in Fig. 6. This is because the illumination falling in the red regions can ensure the point Q is within $P(\mathbf{u}+\mathbf{u_j}) = 1$, and the illumination falling in the blue regions can ensure the point $Q(\mathbf{u})$ is within $P(\mathbf{u}-\mathbf{u_j}) = 1$. However, it should be noted that when the illumination angle is close to the central axis of the objective lens, the two red and blue regions corresponding to $P(\mathbf{u}+\mathbf{u_j})$ and $P(\mathbf{u}-\mathbf{u_j})$ will partially cancel out each other. So the integral interval should be partitioned according to the location of point Q [see Figs. 6(a) and 6(b)], which can be represented as (taking the left–right axis illumination, for example)

$$\mathrm{PTF}_{lr}(\rho,\theta) = \begin{cases} \dfrac{2\int_{\rho-\mathrm{NA_{obj}}}^{\mathrm{NA_{obj}}}\int_{\theta-\alpha}^{\theta+\alpha} S_{lr}(\xi,\varepsilon)\mathrm{d}\varepsilon\mathrm{d}\xi}{\int_{0}^{\mathrm{NA_{obj}}}\int_{0}^{2\pi}|S_{lr}(\xi,\varepsilon)|\mathrm{d}\varepsilon\mathrm{d}\xi} & \mathrm{NA_{obj}} \le \rho \le 2\mathrm{NA_{obj}} \\ \dfrac{2\int_{\mathrm{NA_{obj}}-\rho}^{\mathrm{NA_{obj}}}\int_{\theta-\alpha}^{\theta+\alpha} S_{lr}(\xi,\varepsilon)\mathrm{d}\varepsilon\mathrm{d}\xi}{\int_{0}^{\mathrm{NA_{obj}}}\int_{0}^{2\pi}|S_{lr}(\xi,\varepsilon)|\mathrm{d}\varepsilon\mathrm{d}\xi} & 0 \le \rho < \mathrm{NA_{obj}} \end{cases}. \tag{A2}$$

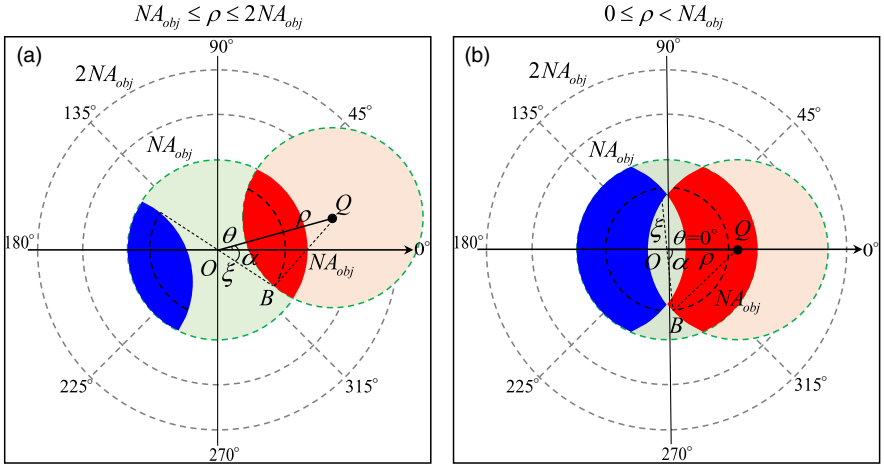

Fig. 6. Schematic diagram of the integral for PTF along the left–right axis illumination in the polar coordinate system. (a) The radius ρ of the point Q is in the range of $\mathrm{NA_{obj}} \le \rho \le 2\mathrm{NA_{obj}}$. (b) The radius ρ of the point Q is in the range of $0 \le \rho < \mathrm{NA_{obj}}$.

Substituting Eq. (A1) into Eq. (A2) gives the PTF along the left–right axis direction:

$$\mathrm{PTF}_{lr}(\rho,\theta)=\begin{cases}\dfrac{\sum_{n=1}^{\infty}a_n\cos(n\theta)\int_{\rho-\mathrm{NA}_{\mathrm{obj}}}^{\mathrm{NA}_{\mathrm{obj}}}L(\xi)\sin(n\alpha)\mathrm{d}\xi}{n\sum_{n=1}^{\infty}a_n\int_0^{\mathrm{NA}_{\mathrm{obj}}}L(\xi)\mathrm{d}\xi} & \mathrm{NA}_{\mathrm{obj}}\le\rho\le 2\mathrm{NA}_{\mathrm{obj}}\\ \dfrac{\sum_{n=1}^{\infty}a_n\cos(n\theta)\int_{\mathrm{NA}_{\mathrm{obj}}-\rho}^{\mathrm{NA}_{\mathrm{obj}}}L(\xi)\sin(n\alpha)\mathrm{d}\xi}{n\sum_{n=1}^{\infty}a_n\int_0^{\mathrm{NA}_{\mathrm{obj}}}L(\xi)\mathrm{d}\xi} & 0\le\rho<\mathrm{NA}_{\mathrm{obj}}\end{cases},$$

$$\mathrm{PTF}_{ud}(\rho,\theta)=\begin{cases}\dfrac{\sum_{n=1}^{\infty}b_n\sin(n\theta)\int_{\rho-\mathrm{NA}_{\mathrm{obj}}}^{\mathrm{NA}_{\mathrm{obj}}}L(\xi)\sin(n\alpha)\mathrm{d}\xi}{n\sum_{n=1}^{\infty}b_n\int_0^{\mathrm{NA}_{\mathrm{obj}}}L(\xi)\mathrm{d}\xi} & \mathrm{NA}_{\mathrm{obj}}\le\rho\le 2\mathrm{NA}_{\mathrm{obj}}\\ \dfrac{\sum_{n=1}^{\infty}b_n\sin(n\theta)\int_{\mathrm{NA}_{\mathrm{obj}}-\rho}^{\mathrm{NA}_{\mathrm{obj}}}L(\xi)\sin(n\alpha)\mathrm{d}\xi}{n\sum_{n=1}^{\infty}b_n\int_0^{\mathrm{NA}_{\mathrm{obj}}}L(\xi)\mathrm{d}\xi} & 0\le\rho<\mathrm{NA}_{\mathrm{obj}}\end{cases}. \tag{A3}$$

The above $\mathrm{PTF}_{lr}(\rho,\theta)$ and $\mathrm{PTF}_{ud}(\rho,\theta)$ are further squared and summed to obtain the synthetic square of amplitude of the multi-axial PTFs by $C(\rho,\theta)=|\mathrm{PTF}_{lr}(\rho,\theta)|^2+|\mathrm{PTF}_{ud}(\rho,\theta)|^2$. Isotropic DPC requires $C(\rho,\theta)$ to be a function only about ρ, which means that there are no cross-trigonometric terms in $C(\rho,\theta)$, suggesting that there should be only one single-harmonic component in the Fourier series expansion of Eq. (A1). It should also be noted that when n is even, the illumination pattern is centrosymmetric so that the resulting PTF will be completely canceled out. Therefore, n should be an odd number ($n=1,3,5,\ldots$) to guarantee a valid non-zero PTF. As a result, the illumination functions $S_{lr}(\rho,\theta)$ and $S_{ud}(\rho,\theta)$ can be deduced as

$$\begin{matrix}S_{lr}(\rho,\theta)=L(\rho)\cos(n\theta)\\ S_{ud}(\rho,\theta)=L(\rho)\sin(n\theta)\end{matrix}\ (n=1,3,5,\ldots). \tag{A4}$$

Note that in Eq. (A4), we neglect the unimportant constant factors. Following this step, the corresponding PTFs can be significantly simplified as follows:

$$\mathrm{PTF}_{lr}(\rho,\theta)=\begin{cases}\cos(n\theta)\dfrac{\int_{\rho-\mathrm{NA}_{\mathrm{obj}}}^{\mathrm{NA}_{\mathrm{obj}}}L(\xi)\sin(n\alpha)\mathrm{d}\xi}{n\int_0^{\mathrm{NA}_{\mathrm{obj}}}L(\xi)\mathrm{d}\xi} & \mathrm{NA}_{\mathrm{obj}}\le\rho\le 2\mathrm{NA}_{\mathrm{obj}}\\ \cos(n\theta)\dfrac{\int_{\mathrm{NA}_{\mathrm{obj}}-\rho}^{\mathrm{NA}_{\mathrm{obj}}}L(\xi)\sin(n\alpha)\mathrm{d}\xi}{n\int_0^{\mathrm{NA}_{\mathrm{obj}}}L(\xi)\mathrm{d}\xi} & 0\le\rho<\mathrm{NA}_{\mathrm{obj}}\end{cases},$$

$$\mathrm{PTF}_{ud}(\rho,\theta)=\begin{cases}\sin(n\theta)\dfrac{\int_{\rho-\mathrm{NA}_{\mathrm{obj}}}^{\mathrm{NA}_{\mathrm{obj}}}L(\xi)\sin(n\alpha)\mathrm{d}\xi}{n\int_0^{\mathrm{NA}_{\mathrm{obj}}}L(\xi)\mathrm{d}\xi} & \mathrm{NA}_{\mathrm{obj}}\le\rho\le 2\mathrm{NA}_{\mathrm{obj}}\\ \sin(n\theta)\dfrac{\int_{\mathrm{NA}_{\mathrm{obj}}-\rho}^{\mathrm{NA}_{\mathrm{obj}}}L(\xi)\sin(n\alpha)\mathrm{d}\xi}{n\int_0^{\mathrm{NA}_{\mathrm{obj}}}L(\xi)\mathrm{d}\xi} & 0\le\rho<\mathrm{NA}_{\mathrm{obj}}\end{cases}. \tag{A5}$$

To further simplify the expression, we define a new function $M(\rho)$ to represent the integral term:

$$M(\rho)=\begin{cases}\dfrac{\int_{\rho-\mathrm{NA}_{\mathrm{obj}}}^{\mathrm{NA}_{\mathrm{obj}}}L(\xi)\sin(n\alpha)\mathrm{d}\xi}{n\int_0^{\mathrm{NA}_{\mathrm{obj}}}L(\xi)\mathrm{d}\xi} & \mathrm{NA}_{\mathrm{obj}}\le\rho\le 2\mathrm{NA}_{\mathrm{obj}}\\ \dfrac{\int_{\mathrm{NA}_{\mathrm{obj}}-\rho}^{\mathrm{NA}_{\mathrm{obj}}}L(\xi)\sin(n\alpha)\mathrm{d}\xi}{n\int_0^{\mathrm{NA}_{\mathrm{obj}}}L(\xi)\mathrm{d}\xi} & 0\le\rho<\mathrm{NA}_{\mathrm{obj}}\end{cases}, \tag{A6}$$

where α is a variable determined by ρ. From the geometric relationship of the triangle BOQ in Fig. 6, we have $\cos\alpha=\frac{\rho^2+\xi^2-\mathrm{NA}_{\mathrm{obj}}^2}{2\rho\xi}$, so $M(\rho)$ here is a function only about ρ. Thus $\mathrm{PTF}_{lr}(\rho,\theta)$ and $\mathrm{PTF}_{ud}(\rho,\theta)$ can be expressed as $\mathrm{PTF}_{lr}(\rho,\theta)=\sin(n\theta)M(\rho)$, and $\mathrm{PTF}_{ud}(\rho,\theta)=\cos(n\theta)M(\rho)$. We can get the expression of $C(\rho,\theta)$ as

$$C(\rho,\theta)=M(\rho)^2. \tag{A7}$$

This result shows that $C(\rho,\theta)$ is independent of θ, suggesting that the distribution of $C(\rho,\theta)$ is circularly symmetric. Therefore, we can conclude that the necessary and sufficient conditions for DPC to achieve a perfectly isotropic PTF is that the illumination function should be in the form of $S_{lr}(\rho,\theta)=L(\rho)\sin(n\theta)$ and $S_{ud}(\rho,\theta)=L(\rho)\cos(n\theta)$, where $L(\rho)$ is an arbitrary function of ρ. This conclusion provides great convenience for the illumination design of isotropic DPC. However, it should be noted that Eq. (A6) generally has no analytical solution, so the PTFs of different patterns can only be evaluated based on numerical simulations.

APPENDIX B: COMPARISON OF DIFFERENT ILLUMINATION SCHEMES FOR ISOTROPIC DPC

Since no restrictions were imposed on the form of the function $L(\rho)$, $L(\rho)$ can be any function of ρ without affecting the isotropy of the DPC's PTF. Thus, we can optimize the function $L(\rho)$ to improve the frequency coverage and response of the corresponding PTF. In this section, we compare the PTFs of three different functions $L(\rho)$: constant weight, linear weight, and Kronecker delta weight functions with a fixed $n=1$ by simulation, as shown in Figs. 7(a1)–7(a3). The PTFs along the left–right axis under different illumination patterns are displayed in Figs. 7(b1)–7(b3). It can be seen the PTF with $L_3(\rho)$ produces the PTF with the highest response at almost all frequencies from 0 to $2\mathrm{NA}_{\mathrm{obj}}$. The results can be seen more clearly from the amplitude of $C(\rho,\theta)$ shown in Figs. 7(c1)–7(c3). To quantitatively characterize the amplitude of these three $C(\rho,\theta)$, the responses along the black cross section are extracted and compared in Fig. 7(d). Although these three illumination patterns can all obtain isotropic $C(\rho,\theta)$,

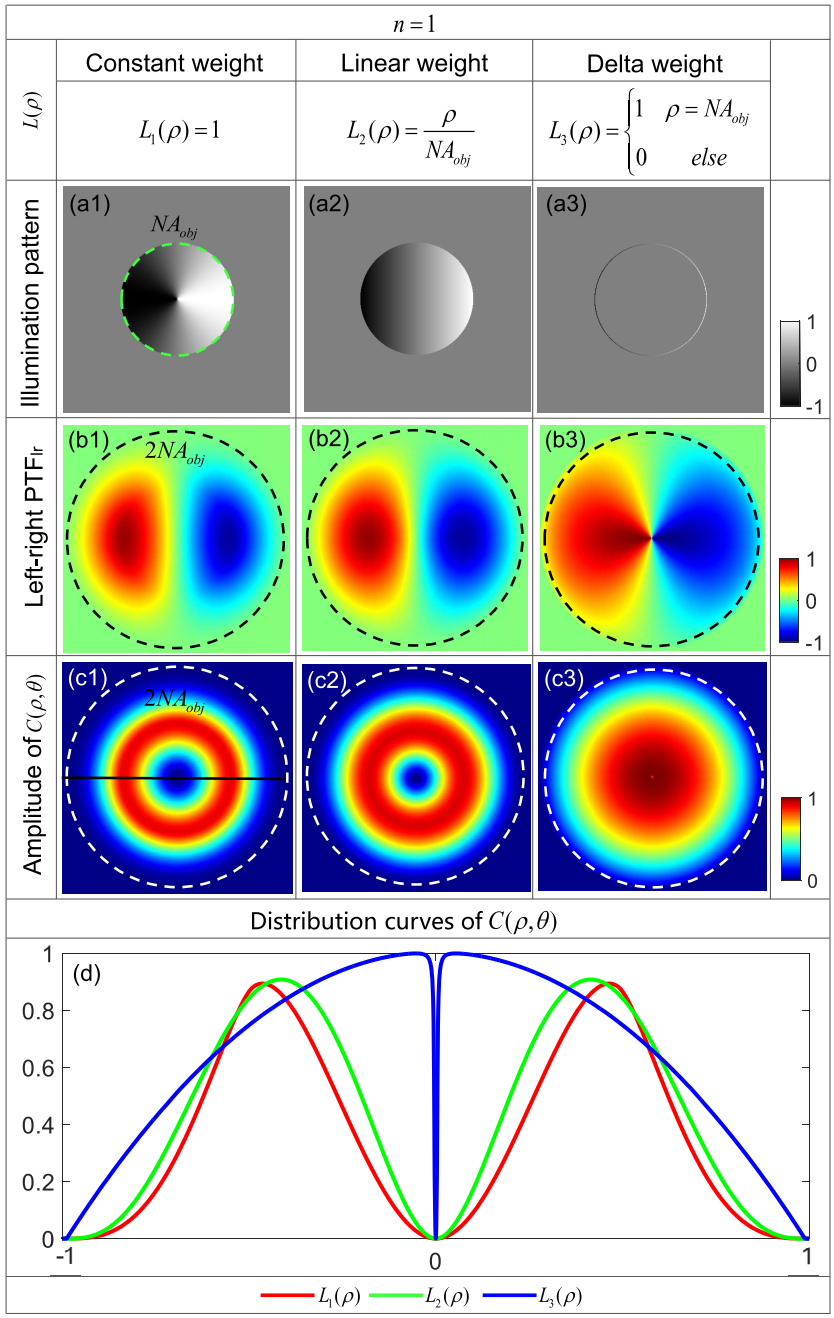

Fig. 7. PTF and $C(\rho,\theta)$ with a different $L(\rho)$ function. (a1)–(a3) Illumination patterns. (b1)–(b3) PTFs along the left–right axis. (c1)–(c3) $C(\rho,\theta)$ with two-axis illumination. (d) Quantitative curves of $C(\rho,\theta)$ along the black line.

a PTF corresponding to $L_3(\rho)$ (a thin annulus) has the highest response at almost all frequencies from 0 to $2\mathrm{NA}_{\mathrm{obj}}$.

APPENDIX C: ANALYSIS OF THE ANNULAR THICKNESS INFLUENCE ON THE FREQUENCY RESPONSES OF PTF

We next analyze the effect of the thickness of the annulus on the PTF by fixing the illumination numerical aperture (NA) of the outer circles to be $\mathrm{NA}_{\mathrm{obj}}$ and only changing the thickness of the annulus ($\sigma = \frac{\mathrm{NA}_{\mathrm{ill}}}{\mathrm{NA}_{\mathrm{obj}}}$). As shown in Figs. 8(b1)–8(b3), when the illumination annulus becomes wide, the frequency responses of the PTF are gradually weakened, especially at low and high frequencies. For the synthetic square of amplitude of the multi-axial PTFs $C(\rho,\theta)$ shown in Figs. 8(c1)–8(c3), it can be observed that a wider annulus attenuates the response near the zero frequency and the high-frequency components approaching $2\mathrm{NA}_{\mathrm{obj}}$. When $\sigma \to 0$, it can be expected that the phase response finally approaches that of the constant weight function $L(\rho) = 1$ [Figs. 7(a1)–7(c1) are reproduced].

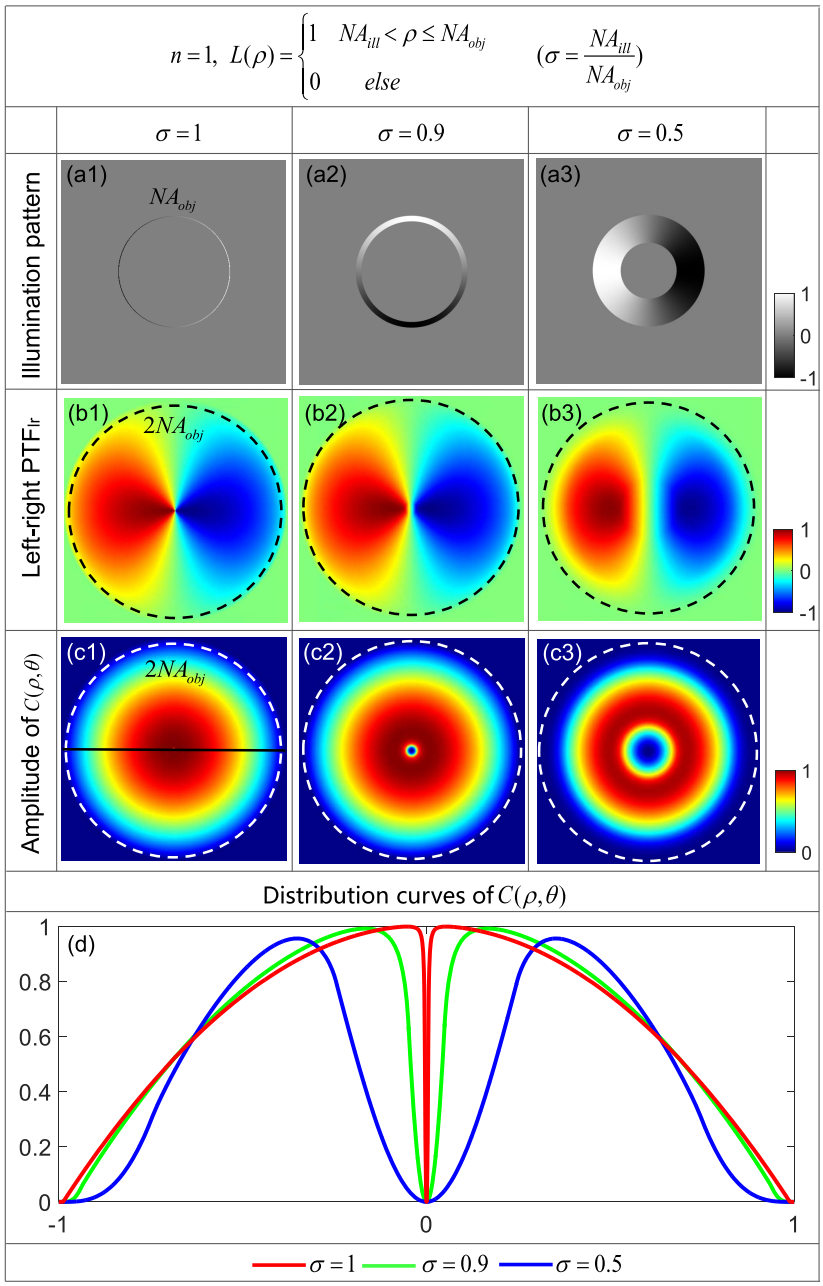

Fig. 8. PTF and $C(\rho,\theta)$ with different thickness of the annulus (three σ). (a1)–(a3) Illumination patterns. (b1)–(b3) PTFs along the left–right axis. (c1)–(c3) $C(\rho,\theta)$ with two-axis illumination. (d) Quantitative curves of $C(\rho,\theta)$ along the black line.

This is because the paraxial illumination does not produce low-frequency phase contrast, and only illumination matching the objective NA_{obj} can produce the strong response at all frequencies. From the results shown in Fig. 8, it can be deduced that we should choose the diameter of the annulus to be equal to that of the objective pupil and make its thickness as small as possible [i.e., the Kronecker delta weight function, $\delta(\rho - NA_{obj})$] to optimize the response of PTF. However, in a practical imaging system, the width of the annulus cannot be infinitesimally thin. From the results shown in Fig. 8(c1) and Fig. 8(c2), it can be found that although $C(\rho,\theta)$ corresponding to $\sigma = 0.9$ is slightly inferior to that obtained when $\sigma = 1$, it can still ensure a relatively strong response over a broad frequency range while the light throughput can be much improved.

APPENDIX D: ANALYSIS OF INFLUENCE OF PERIODICITY OF THE ILLUMINATION FUNCTION ON THE FREQUENCY RESPONSES OF PTF

Finally, to analyze the effect of number n in Eq. (A4) on the PTF, the same $L(\rho)$ function and different n are adopted to generate three illumination patterns, as shown in Figs. 9(a1)–9(a3). The PTFs obtained under these three

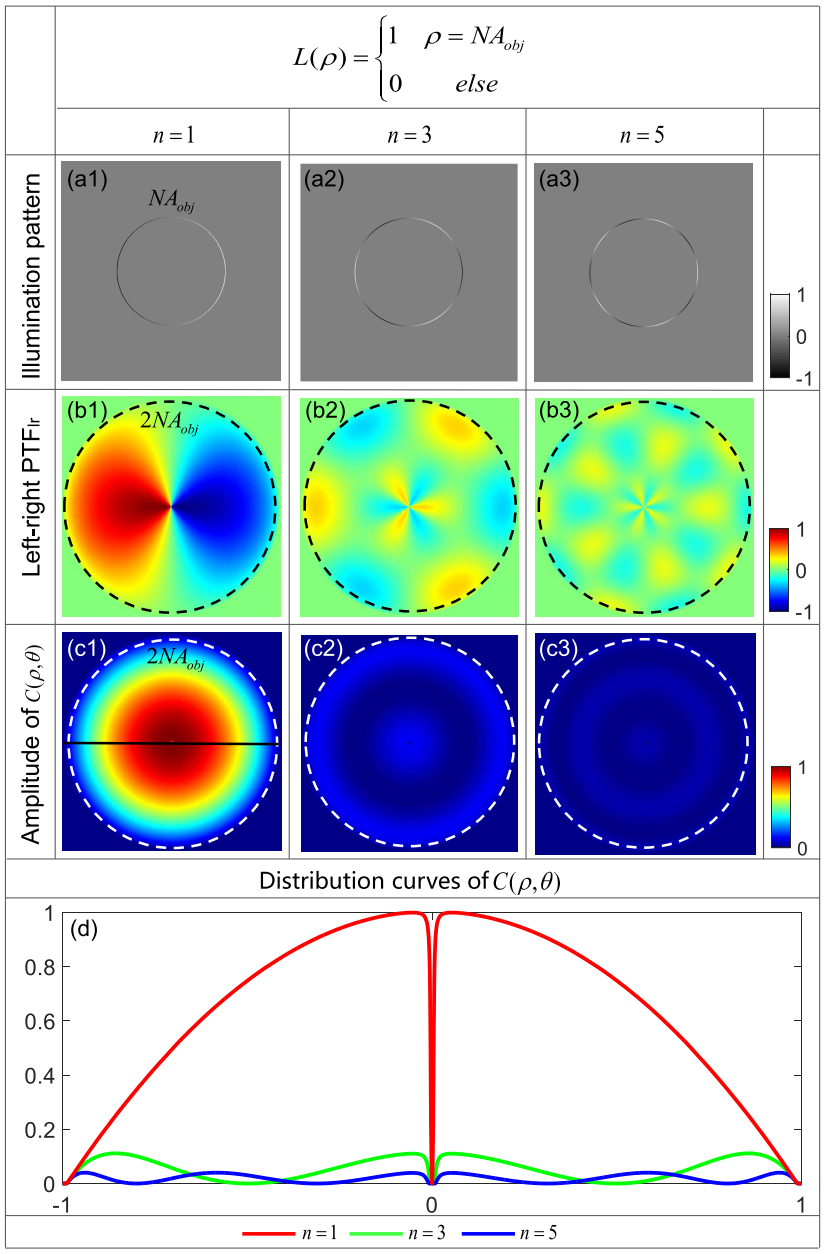

Fig. 9. PTF and $C(\rho,\theta)$ with a different n. (a1)–(a3) Illumination patterns. (b1)–(b3) PTFs along the left–right axis. (c1)–(c3) $C(\rho,\theta)$ with two-axis illumination. (d) Quantitative curves of $C(\rho,\theta)$ along the black line.

illumination patterns are presented in Figs. 9(b1)–9(b3). It is shown that when n increases ($n = 3, 5$), not only the PTF response is significantly attenuated, but also the number of zero crossings in $C(\rho,\theta)$ increases. This is because the increase of n causes more changes of periods for the illumination pattern, resulting in a large number of positive and negative apertures to cancel each other out, so that only a PTF with a very weak response can be obtained. In such cases, the phase information of the sample is hardly transmitted into the intensity, and the reconstruction phase can be severely distorted due to the ill-posedness of the PTF inversion. Thus, we can conclude that $n = 1$ provides the optimal PTF for DPC with the strongest response and no zero crossings from 0 to $2\mathrm{NA}_{\mathrm{obj}}$.

APPENDIX E: PERFORMANCE ANALYSIS OF OPTIMAL ILLUMINATION SCHEME WITH OPTICAL ABERRATION

Generally, the real imaging system includes optical aberrations. In Appendix E, we evaluate the performance of the optimal illumination scheme with optical aberration by simulating DPC-captured images with an additional pupil aberration error. As shown in Figs. 10(a1)–10(f1), different levels of aberrations are introduced to the DPC imaging system to generate captured images. These images are used to achieve phase reconstruction. If the system aberration is not pre-measured, but the ideal PTF is directly used to implement the

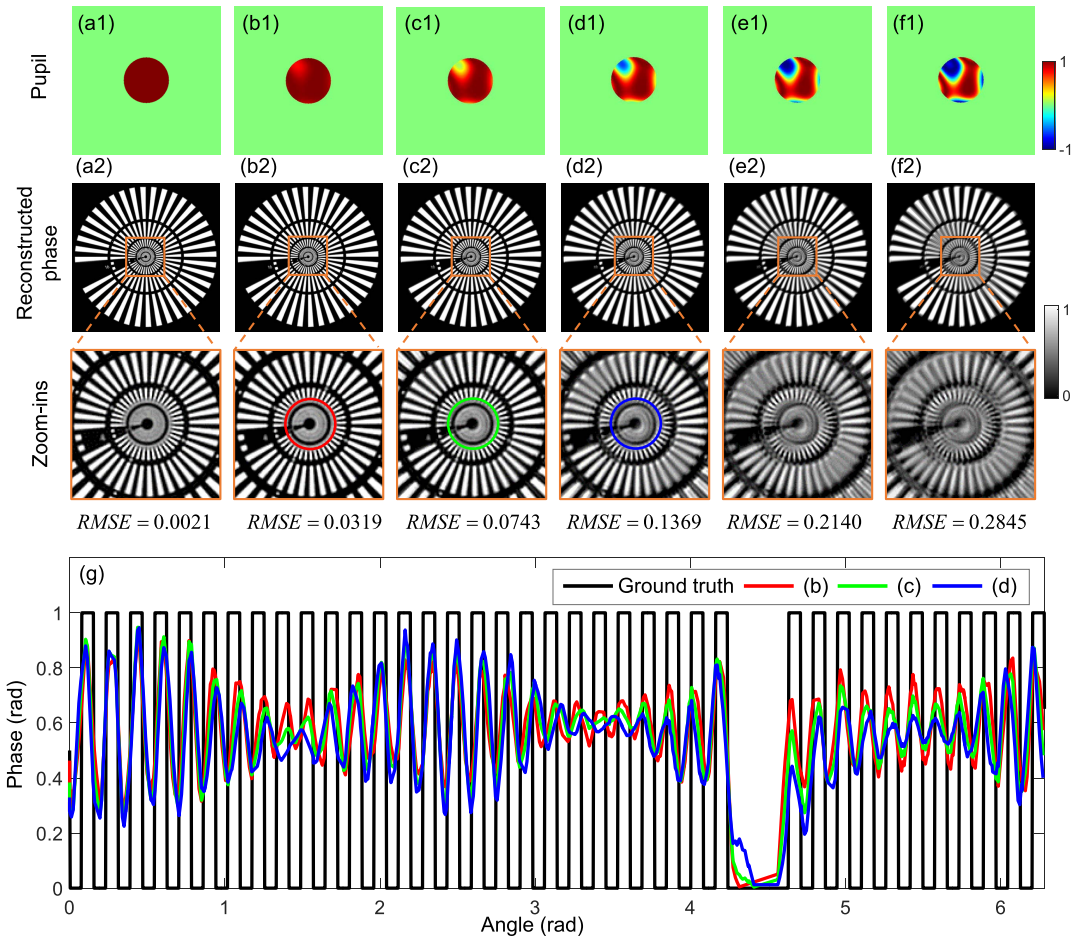

Fig. 10. Simulation results of the optimal illumination scheme with different aberration levels. (a1)–(f1) Pupil with different aberration levels. (a2)–(f2) Reconstruction phase. (g) Quantitative curves of the reconstruction phase.

phase reconstruction, the reconstructed phase is shown in Figs. 10(a2)–10(f2). The zoom-ins of the smallest features are displayed to compare the effects of different level aberrations on the phase reconstruction results. It can be observed that when the aberration is not big [Figs. 10(a2)–10(c2)], a stable correct reconstruction phase can still be obtained. As the aberration increases, the errors and artifacts in the phase results become larger. We further extract and plot the phase value at the diffraction limit resolution in Figs. 10(b2)–10(d2), as shown in Fig. 10(g). Although the phase contrast of this resolution in different directions is reduced to varying degrees due to the influence of the aberration, the diffraction limit resolution of Figs. 10(b2)–10(c2) still can be clearly distinguished. Thus, we can conclude that a high-quality reconstructed phase can still be obtained with optimal illumination when the system aberration is not very large. In systems with large aberrations, it is necessary to eliminate them by means of aberration compensation [39].

Funding. National Natural Science Foundation of China (NSFC) (61722506, 11574152); Final Assembly "13th Five-Year Plan" Advanced Research Project of China (30102070102); Equipment Advanced Research Fund of China (61404150202); National Defense Science and Technology Foundation of China (0106173); Outstanding Youth Foundation of Jiangsu Province of China (BK20170034); Key Research and Development Program of Jiangsu Province (BE2017162); "333 Engineering" Research Project of Jiangsu Province (BRA2016407); Fundamental Research Funds for the Central Universities (30917011204); Open Research Fund of Jiangsu Key Laboratory of Spectral Imaging & Intelligent Sense (3091801410411).

†These authors contributed equally to this work.

REFERENCES

1. G. Popescu, *Quantitative Phase Imaging of Cells and Tissues* (McGraw Hill Professional, 2011).
2. A. Barty, K. Nugent, D. Paganin, and A. Roberts, "Quantitative optical phase microscopy," Opt. Lett. **23**, 817–819 (1998).
3. E. Cuche, F. Bevilacqua, and C. Depeursinge, "Digital holography for quantitative phase-contrast imaging," Opt. Lett. **24**, 291–293 (1999).
4. Y. Kim, H. Shim, K. Kim, H. Park, S. Jang, and Y. Park, "Profiling individual human red blood cells using common-path diffraction optical tomography," Sci. Rep. **4**, 6659 (2014).
5. G. Popescu, "Quantitative phase imaging of nanoscale cell structure and dynamics," Methods Cell Biol. **90**, 87–115 (2008).

6. C. J. Mann, L. Yu, C.-M. Lo, and M. K. Kim, "High-resolution quantitative phase-contrast microscopy by digital holography," Opt. Express **13**, 8693–8698 (2005).
7. P. Marquet, B. Rappaz, P. J. Magistretti, E. Cuche, Y. Emery, T. Colomb, and C. Depeursinge, "Digital holographic microscopy: a noninvasive contrast imaging technique allowing quantitative visualization of living cells with subwavelength axial accuracy," Opt. Lett. **30**, 468–470 (2005).
8. B. Kemper and G. von Bally, "Digital holographic microscopy for live cell applications and technical inspection," Appl. Opt. **47**, A52–A61 (2008).
9. M. R. Teague, "Deterministic phase retrieval: a Green's function solution," J. Opt. Soc. Am. **73**, 1434–1441 (1983).
10. S. S. Kou, L. Waller, G. Barbastathis, and C. J. Sheppard, "Transport-of-intensity approach to differential interference contrast (TI-DIC) microscopy for quantitative phase imaging," Opt. Lett. **35**, 447–449 (2010).
11. J. C. Petruccelli, L. Tian, and G. Barbastathis, "The transport of intensity equation for optical path length recovery using partially coherent illumination," Opt. Express **21**, 14430–14441 (2013).
12. C. Zuo, Q. Chen, W. Qu, and A. Asundi, "High-speed transport-of-intensity phase microscopy with an electrically tunable lens," Opt. Express **21**, 24060–24075 (2013).
13. C. Zuo, Q. Chen, W. Qu, and A. Asundi, "Noninterferometric single-shot quantitative phase microscopy," Opt. Lett. **38**, 3538–3541 (2013).
14. C. Zuo, Q. Chen, Y. Yu, and A. Asundi, "Transport-of-intensity phase imaging using Savitzky–Golay differentiation filter-theory and applications," Opt. Express **21**, 5346–5362 (2013).
15. F. Pfeiffer, T. Weitkamp, O. Bunk, and C. David, "Phase retrieval and differential phase-contrast imaging with low-brilliance X-ray sources," Nat. Phys. **2**, 258–261 (2006).
16. D. Hamilton and C. Sheppard, "Differential phase contrast in scanning optical microscopy," J. Microsc. **133**, 27–39 (1984).
17. B. Kachar, "Asymmetric illumination contrast: a method of image formation for video light microscopy," Science **227**, 766–768 (1985).
18. S. B. Mehta and C. J. Sheppard, "Quantitative phase-gradient imaging at high resolution with asymmetric illumination-based differential phase contrast," Opt. Lett. **34**, 1924–1926 (2009).
19. L. Tian, J. Wang, and L. Waller, "3d differential phase-contrast microscopy with computational illumination using an LED array," Opt. Lett. **39**, 1326–1329 (2014).
20. L. Tian and L. Waller, "Quantitative differential phase contrast imaging in an LED array microscope," Opt. Express **23**, 11394–11403 (2015).
21. G. Zheng, R. Horstmeyer, and C. Yang, "Wide-field, high-resolution Fourier ptychographic microscopy," Nat. Photonics **7**, 739–745 (2013).
22. X. Ou, R. Horstmeyer, C. Yang, and G. Zheng, "Quantitative phase imaging via Fourier ptychographic microscopy," Opt. Lett. **38**, 4845–4848 (2013).
23. L. Tian, X. Li, K. Ramchandran, and L. Waller, "Multiplexed coded illumination for Fourier ptychography with an LED array microscope," Biomed. Opt. Express **5**, 2376–2389 (2014).
24. C. Zuo, J. Sun, and Q. Chen, "Adaptive step-size strategy for noise-robust Fourier ptychographic microscopy," Opt. Express **24**, 20724–20744 (2016).
25. J. Sun, C. Zuo, L. Zhang, and Q. Chen, "Resolution-enhanced Fourier ptychographic microscopy based on high-numerical-aperture illuminations," Sci. Rep. **7**, 1187 (2017).
26. C. Zuo, J. Sun, J. Li, J. Zhang, A. Asundi, and Q. Chen, "High-resolution transport-of-intensity quantitative phase microscopy with annular illumination," Sci. Rep. **7**, 7654 (2017).
27. J. Li, Q. Chen, J. Sun, J. Zhang, X. Pan, and C. Zuo, "Optimal illumination pattern for transport-of-intensity quantitative phase microscopy," Opt. Express **26**, 27599–27614 (2018).
28. J. Sun, C. Zuo, J. Zhang, Y. Fan, and Q. Chen, "High-speed Fourier ptychographic microscopy based on programmable annular illuminations," Sci. Rep. **8**, 7669 (2018).
29. J. Sun, Q. Chen, Y. Zhang, and C. Zuo, "Efficient positional misalignment correction method for Fourier ptychographic microscopy," Biomed. Opt. Express **7**, 1336–1350 (2016).
30. D. Lee, S. Ryu, U. Kim, D. Jung, and C. Joo, "Color-coded LED microscopy for multi-contrast and quantitative phase-gradient imaging," Biomed. Opt. Express **6**, 4912–4922 (2015).
31. C. Zuo, J. Sun, S. Feng, M. Zhang, and Q. Chen, "Programmable aperture microscopy: a computational method for multi-modal phase contrast and light field imaging," Opt. Lasers Eng. **80**, 24–31 (2016).
32. W. Lee, D. Jung, S. Ryu, and C. Joo, "Single-exposure quantitative phase imaging in color-coded LED microscopy," Opt. Express **25**, 8398–8411 (2017).
33. Z. F. Phillips, M. Chen, and L. Waller, "Single-shot quantitative phase microscopy with color-multiplexed differential phase contrast (cDPC)," PLoS ONE **12**, e0171228 (2017).
34. M. Kellman, M. Chen, Z. F. Phillips, M. Lustig, and L. Waller, "Motion-resolved quantitative phase imaging," Biomed. Opt. Express **9**, 5456–5466 (2018).
35. Y.-Z. Lin, K.-Y. Huang, and Y. Luo, "Quantitative differential phase contrast imaging at high resolution with radially asymmetric illumination," Opt. Lett. **43**, 2973–2976 (2018).
36. H.-H. Chen, Y.-Z. Lin, and Y. Luo, "Isotropic differential phase contrast microscopy for quantitative phase bio-imaging," J. Biophoton. **11**, e201700364 (2018).
37. A. Robey and V. Ganapati, "Optimal physical preprocessing for example-based super-resolution," Opt. Express **26**, 31333–31350 (2018).
38. M. Kellman, E. Bostan, N. Repina, and L. Waller, "Physics-based learned design: optimized coded-illumination for quantitative phase imaging," IEEE Trans. Comput. Imaging (to be published).
39. M. Chen, Z. F. Phillips, and L. Waller, "Quantitative differential phase contrast (DPC) microscopy with computational aberration correction," Opt. Express **26**, 32888–32899 (2018).
40. H. Rose, "Nonstandard imaging methods in electron microscopy," Ultramicroscopy **2**, 251–267 (1976).
41. D. Hamilton, C. Sheppard, and T. Wilson, "Improved imaging of phase gradients in scanning optical microscopy," J. Microsc. **135**, 275–286 (1984).
42. J. Sun, Q. Chen, J. Zhang, Y. Fan, and C. Zuo, "Single-shot quantitative phase microscopy based on color-multiplexed Fourier ptychography," Opt. Lett. **43**, 3365–3368 (2018).
43. C. J. Sheppard, S. Roth, R. Heintzmann, M. Castello, G. Vicidomini, R. Chen, X. Chen, and A. Diaspro, "Interpretation of the optical transfer function: significance for image scanning microscopy," Opt. Express **24**, 27280–27287 (2016).
44. M. Bertero and P. Boccacci, *Introduction to Inverse Problem in Imaging* (CRC Press, 1998).
45. Y. Fan, J. Sun, Q. Chen, J. Zhang, and C. Zuo, "Wide-field anti-aliased quantitative differential phase contrast microscopy," Opt. Express **26**, 25129–25146 (2018).
46. R. Horstmeyer, R. Heintzmann, G. Popescu, L. Waller, and C. Yang, "Standardizing the resolution claims for coherent microscopy," Nat. Photonics **10**, 68–71 (2016).
47. C. Zuo, J. Sun, S. Feng, Y. Hu, and Q. Chen, "Programmable colored illumination microscopy (PCIM): a practical and flexible optical staining approach for microscopic contrast enhancement," Opt. Lasers Eng. **78**, 35–47 (2016).